Interference coupling mechanisms in Silicon Strip Detectors - CMS tracker "wings": A learned lesson for SLHC -

F. Arteche [a], C. Esteban [a], C. Rivetta [b,]

[a] Instituto Tecnológico de Aragón (ITA), Zaragoza, Spain
[b] SLAC National Accelerator Laboratory, Stanford University, USA

farteche@ita.es

Abstract

The identification of coupling mechanisms between noise sources and sensitive areas of the front-end electronics (FEE) in the previous CMS tracker sub-system is critical to optimize the design and integration of integrated circuits, sensors and power distribution circuitry for the proposed SLHC Silicon Strip Tracker systems.

This paper presents a validated model of the noise sensitivity observed in the Silicon Strip Detector-FEE of the CMS tracker that allows quantifying both the impact of the noise coupling mechanisms and the system immunity against electromagnetic interferences. This model has been validated based on simulations using finite element models and immunity tests conducted on prototypes of the Silicon Tracker End-Caps (TEC) and Outer Barrel (TOB) systems. The results of these studies show important recommendations and criteria to be applied in the design of future detectors to increase the immunity against electromagnetic noise.

I. INTRODUCTION

The *Silicon Tracker* is located in the interaction region of the calorimeter and two parts; the inner one based on *Pixel detectors* and the outer part built with *Silicon micro-strip detectors*. In the *silicon tracking* system, the detector module is the basic functional component. Each module consists of three main elements:

- Single or double side silicon micro-strip sensors.
- Mechanical support (Carbon fibre frame).
- Readout front-end electronics (Hybrid circuit).

These modules are grouped, partially overlapped, in leaders and petals to cover several cylinders and end-caps of the tracker's mechanical structure. The hybrid module includes the sensitive front-end amplifier APV25 [1]. Power distribution and slow control signal are distributed to the modules by a custom interconnection board (ICB).

The analysis presented in this paper is based on data measured on the Tracker End-Caps (TEC) and Tracker Outer-Barrel (TOB) detectors. The TEC prototype used to perform the EMC tests consisted of a *'petal'* with 96 APV25 chips and associated electronics distributed along one interconnection board (ICB). The TOB prototype used in the test consisted of a *'leader'* with 6 modules (about 28 APV25) distributed along the ICB. The tracker detector uses similar detector modules, being the main difference among sub-detectors (TEC, TIB, TOB) the geometric arrange of the modules and the ICB design.

Based on the measurements to characterize the electromagnetic interference (EMI) immunity of the tracker FEE, this paper presents a model that describes and quantifies the interference coupling mechanism between the near-field radiated by the ICB and the sensitive areas of the detector module. This coupling mechanism was detected during the EMI immunity tests [2] and was a limiting factor of the FEE noise performance during the tracker integration.

II. EMI CHARACTERIZATION OF TRACKER

Since the tracker FEE is linked to the acquisition system via optical fibres, the conductive noise is mainly coupled into the FEE through the input power cables and the slow control network. To characterize the electromagnetic susceptibility of the FEE to conductive disturbances, different tests are conducted by injecting RF currents through the FEE input power and slow control cables. The main goal of these tests is to characterize the immunity of the system to RF perturbations [3] [4].

A. Test set-up

The experimental set-up is designed [5][6] such that the FEE and the auxiliary equipment exhibit during the test a configuration as close as possible to the final one. The perturbing signal is injected to the FEE input power and slow control cables using a bulk injection current probe, a RF amplifier and a RF signal generator. The level of the injected signal is monitored using an inductive current clamp and a spectrum analyser. The test procedure consists in injecting a sine-wave perturbing current at different frequencies and amplitudes into the FEE through the input cables and evaluating the performance of the FEE, measuring the output noise signal. The output signal of the FEE is measured by its own acquisition system. The frequency range of the injected RF signal is between 150 kHz and 50 MHz.

The data used in this paper to model the coupling mechanism between the ICB and the detector module correspond to the common mode (CM) noise injection. In this case, the perturbation sine-wave current is injected to both the active and return power cables. The sine wave injected will perturb the FEE by adding a noise component to the intrinsic thermal noise component of the APV25. The level of the signal injected is large enough to have a good signal-to-noise ratio at the input of the ADC without affecting the linearity of the overall FEE. The coupled interference to the FEE depends on the amount of noise current induced in the sensitive areas of the FEE.

III. EMI CHARACTERIZATION - RESULTS

Results from tests conducted on prototypes of TEC and TOP detectors give insights to analyze the coupling mechanism between the noise source and the sensitive front-end electronics.

A. Tracker End Cap

Injection signal tests [2] have showed that the noise does not distribute equally among all the channels in the TEC petal tested. The strip channels located in the centre of the silicon detector are more sensitive that those located near the periphery. The detector-APV modules closer to the ICB and petal connector also are more sensitive. The sensitivity to noise or interference increases in frequency from zero at 20-40dB/dec and extend above the intrinsic bandwidth of the APV. The frequency response also includes two resonances associated to parasitic coupling between the ICB and ground connections.

B. Tracker Output Barrel

Results [6] from the TOB showed a non-uniform distribution of the coupled perturbation among the channels of the rod under test. In this case, the strip channels located in the centre of the silicon detector are less sensitive and the most sensitive detector-APV modules are those located close to the rod's input power connector. The frequency response of the coupled noise is similar to the TEC channels, with exception of the resonance frequencies.

Additional tests were performed in TOB in order to analyze the origin and coupling mechanism of the interference. An un-grounded cooper sheet, isolated on one side, with an area approximately equal to ¼ of the silicon detector area was used to screen partially the detector. Partial screening of different detector's areas with the cooper plate gave different results. Covering the areas remote of the pitch adapter did not introduce appreciable noise reduction for all the channels. When the cooper sheet covered the areas over the pitch adapter the interference coupling was null.

This set of tests allows defining the pitch adapter region of the hybrid module and silicon sensor as the area susceptible to near-field interference generated by the ICB. The coupled field should be prominently magnetic, because the effect of the shielding is negligible when the cooper sheet is covering the detector in areas remote from the pitch adapter. If Electric field is the major component of the coupled field, the attenuation due to the screening should be the same for all region of the silicon detector.

IV. NOISE COUPLING

To investigate the coupling mechanism between front-end electronics/silicon detector and the noise generated by the ICB when common mode current are flowing, we separated the study in 3 parts: Noise source or field generation, Sensitive area in the receptor and signal processing in the receptor. The last part it is important to be included in the analysis because the signal measured by the electronic system and used in the analysis is partially processed.

A. Noise Source – Near-Fields

The noise source is controlled in these tests because the interference injected to the ICB is known. The electric and magnetic field around the ICB can be calculated via finite element simulation to have a perfect representation of the electric and magnetic near-field perturbing the silicon detector and the front-end electronics. Results of the magnetic field for the TEC and TOB configurations are depicted in Fig. 1 and 2.

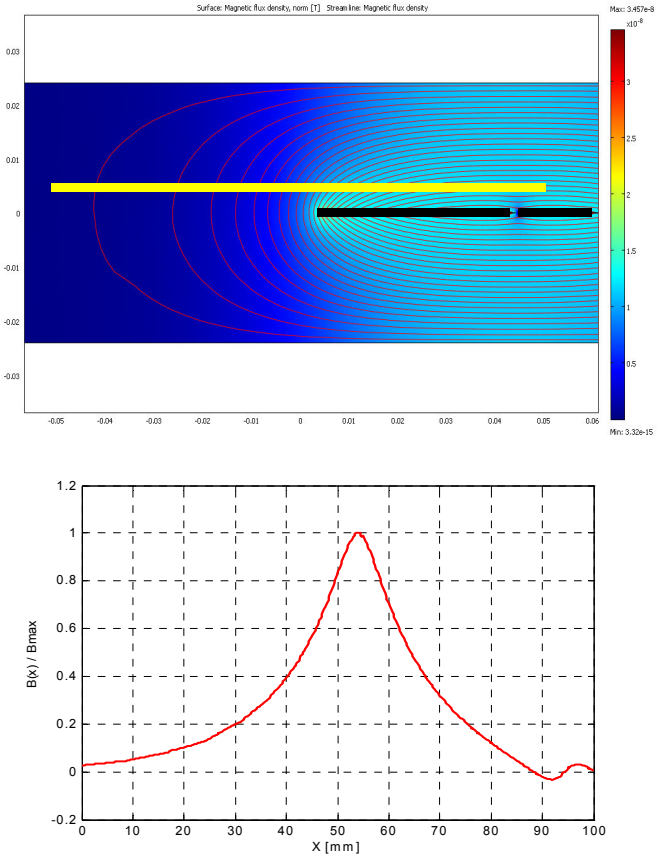

Figure 1: *A:* Magnetic field around the ICB (lower line) and Silicon Detector (upper line) for the TEC module. *B:* Normalized vertical magnetic field component $(By(x)/B_{max})$ around the Silicon detector

The relative position between the ICB and the silicon detector is preserved in the analysis for both cases. The upper plots show a view of the x-y plane for a given location along z in the ICB and the silicon detector. The closed lines represent curves of constant magnetic induction in x-y. Using as reference the position along the width of the silicon detector (x axis, x=0 left edge, x=100 mm right edge), the lower plots depicts the normalized magnitude of the vertical component of the magnetic field $By(x)$ intersecting the silicon detector.

Fig. 1 corresponds to the TEC case and it is possible to observe that the vertical component of the magnetic field intersecting the silicon detector has a maximum at the centre of the device (left edge of ICB). At the left side of the center, it decreases because of the distance, however at the right side, it decreases because the horizontal component of the magnetic field start to be the dominant one. For TOB Fig 2 because the ICB and the silicon detector are mounted one over the other sharing the x symmetry line, the vertical component of the magnetic field is odd-symmetric respect to x=40mm. Similar

results can be obtained for the other near-field components around the silicon detector.

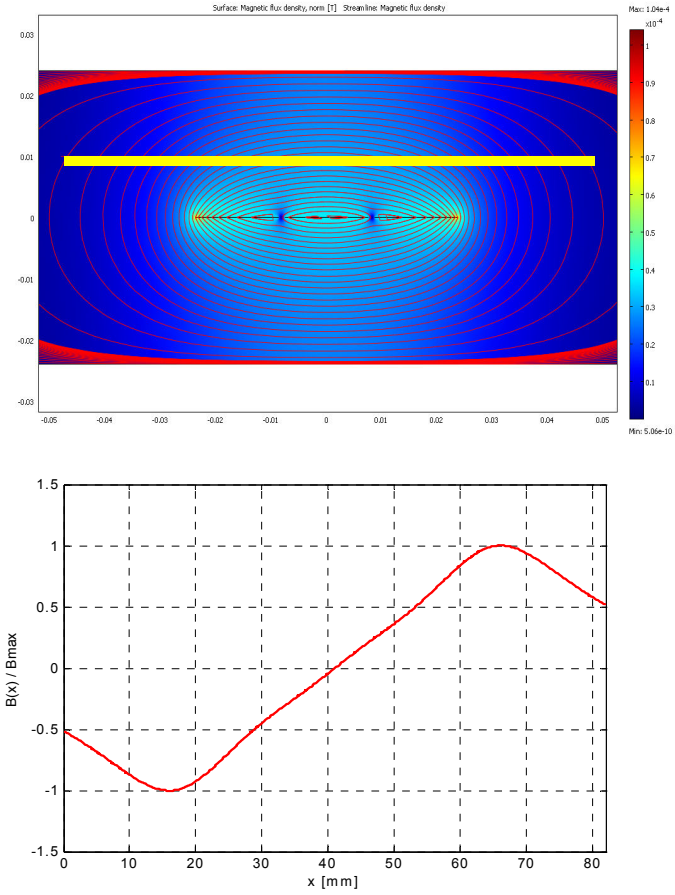

Figure 2: *A:* Magnetic field around the ICB (lower line) and Silicon Detector (upper line) for the TOB module. *B:* Normalized vertical magnetic field component *(By(x)/B_{max})* around the Silicon detector

B. Sensitive area in the receptor

The critical area in the front-end electronics/silicon detector, in general, is the connections between the detector and the sensitive front-end electronics. In that connection, the signal level is the lowest in all the electronic system. Additionally, front-end amplifiers have large gain to be able to process the tinny signals delivered by the HEP detector. The connection between the strips of the silicon detector and the multichannel is simple. Each 512 channel detector is read-out by 4 APVs with 128 channel each one. Each strip is connected to the input pin of the corresponding APV through the wire bonding between the hybrid board and the pitch adapter. To close the signal circuit, the current return circuit has not a direct connection to the hybrid board or APV chips. Currents return via the silicon detector backplane but there is no direct connection between the backplane and the hybrid circuit. From the backplane, currents find the return path through the conductive carbon fibre [7] holder of the detector and through parasitic capacitive find the hybrid board. This signal circuit can be understood better following the electrical and mechanical schemes showed in Figs. 3 and 4. Fig. 3 depicts a simplified electric circuit of the input signal path, showing the main components that define the loop.

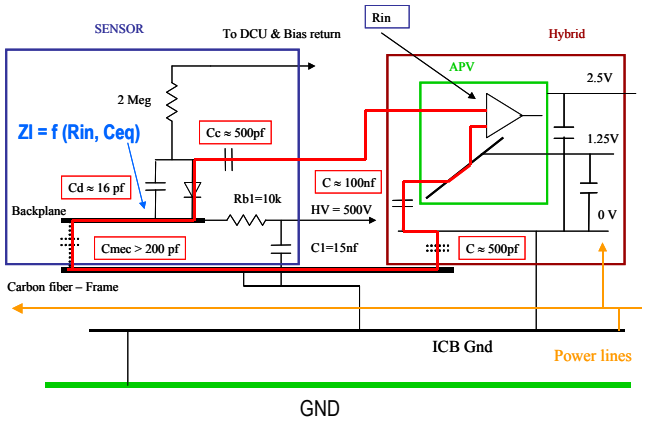

Figure 3: Simplified electric circuit describing the Silicon Detector-APV25 connection.

Signal currents return to the APV flowing through the backplane, the capacitive coupling between the backplane and the carbon fibre, the carbon fibre holder (carbon fibre legs and cross-piece) and the hybrid board. This path is mainly formed by parasitic elements in the circuits, defining not the optimal path compatible with the circuit sensitivity at that point. The main problem associated with the return current path in the pitch adapter area can be explored from in the following figures.

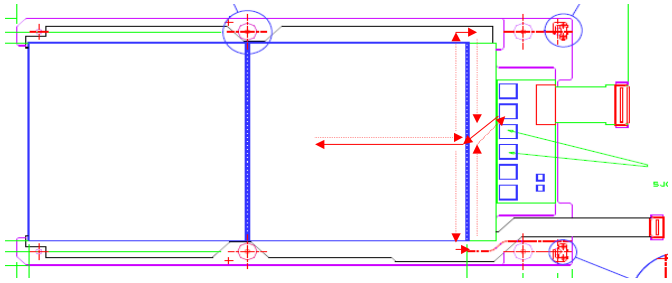

Figure 4: Top view of the detector module: Silicon Detector & Hybrid module

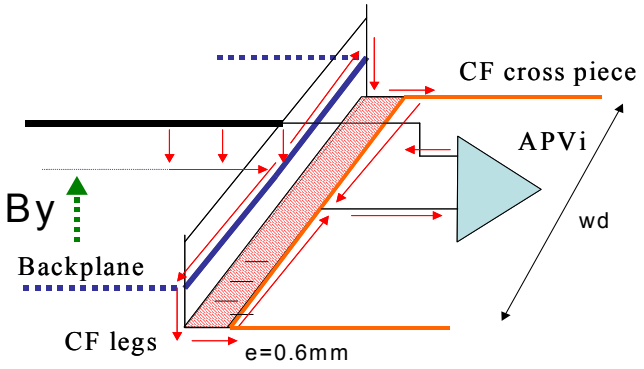

Figure 5: Partial view of the pitch adapter area

Fig 4 shows the top view of the tracker module. From Figs 3 and 4 it is possible to observe that for the current, the lowest impedance path around the pitch adapter is flowing through the edges of the holder structure as defined by the dot lines and arrows. This loop is defined by the no direct connection between the hybrid's 0V layer and the detector backplane. This loop increases the susceptibility of the circuit to vertical magnetic fields (By). A more detailed drawing of that area is

shown in Fig. 5, where it is defined a rectangular loop whose length is equal to the silicon detector width (wd) and the width (e) equal to the gap between the back-plane and the hybrid board (around 0.6mm). This loop is common to the 512 channels of the strip silicon detector.

C. *APV Signal Processing*

The APV [1] is a charge amplifier followed by a shaper able to amplify and process current signals from the strip detector up to a frequency around 10MHz. This processing is the same for all the 128 channels included in the chip. Additionally, each chip includes a common mode (CM) subtraction to reduce the common mode noise induced in the 512 channels of the detector. Therefore, the multi-signal recorded and used for analysis is not proportional to the input current per channel but it includes the coupling of all the other APV's channels due to the common mode subtraction. Defining the input current per APV channel as $i_{APVi}(t)$ with *i=1,2…128* being the channel number, then the output signal $v_{oi}(t)$ is

$$v_{oi}(t) = \int_{-\infty}^{\infty} h_{APV}(t-\tau) * \left[i_{APV}(\tau) - \frac{1}{128} \sum_{i=1}^{128} i_{APV}(\tau) \right] d\tau \qquad (1)$$

where $h_{APV}(t)$ is the impulsive response of each APV channel. Each APV subtracts the common mode level corresponding to 128 channels of the detector, shifting the corresponding DC level of those 128 output signals. For a given silicon detector, the CM level for adjacent APVs can be different.

V. Coupling Mechanism Model

Based on the analysis presented in previous section, the magnetic interference coupled into the input signal loop can be quantized using the simple model depicted in Fig. 6.

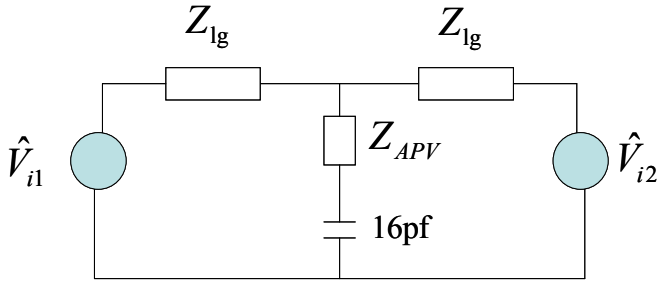

Figure 6: Simplified circuit

The loop showed in Figs. 4 and 5, can be considered as a short transmission line conformed by two conductors (one is the backplane, the other is the CF cross-piece) with capacitive loads at both ends (mechanical joint between the CF legs and CF cross-piece) and illuminated by a perpendicular magnetic field *By*. Between the conductors, the input impedance of the APV is connected through a series capacitor that represents the capacitance between the silicon strip and the backplane. The circuit depicted only shows one of the APV channels and the equivalent voltage generators represent the voltage induced by the magnetic field toward the left and right of the APV channel considered. These equivalent voltages can be expressed as

$$v_{i1}(t) = e\int_{1}^{i} \dot{B}_y(t,x)\,dx, \quad v_{i2}(t) = e\int_{i}^{512} \dot{B}_y(t,x)\,dx \qquad (2)$$

with e: the width of the loop or separation between conductive surfaces (Fig.5) and $\dot{B}_y(t,x) = \frac{dB_y(t,x)}{dt}$. The current flowing through the input impedance of the APV (input current) in frequency domain is

$$I_{APVi}(\omega) = \frac{V_{i1}(\omega) - V_{i2}(\omega)}{Z_{lg} + Z_{APVi}} \qquad (3)$$

Based on the magnetic induction *By(x)* calculated previously for the TEC and TOB configurations, it is possible to evaluate the APV's input current for the 512 channels of the silicon detector. Solving (2) and (3) for a given time t and assuming direct proportionality between I_{APV} and the voltage difference, the input current per channel for both detector are plotted in Fig. 7. The dotted red lines separate the channels processed by each APV.

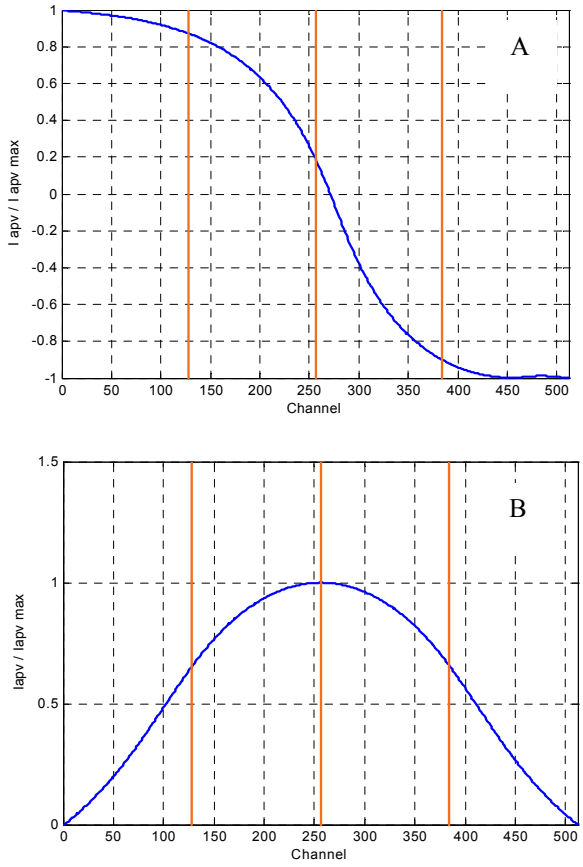

Figure 7: APV normalized current distribution per channel $I_{APVi}/I_{APV\max}$ - *A:* TEC Detector , *Br:* TOB Detector

Considering the effect of the common mode subtraction included in each APV-25, the signal proportional to the output voltage is plotted in Fig 8.

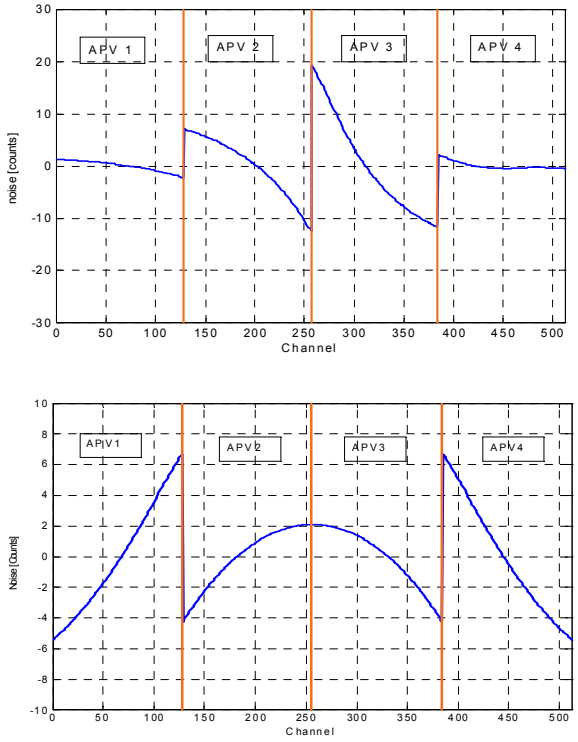

Figure 8: Digitized APV output voltage distribution per channel after common mode subtraction -
A: TEC Detector , *B:* TOB Detector

VI. Results – Comparison between Measurements and Simulations

In order to compare the measurements and the results obtained by simulations based on the model presented, a particular analysis of the recorded data was conducted. If a common mode current is injected to the ICB at a particular frequency, at any time, the measurements and simulation results should give the same voltage distribution for all the APV channels. For a particular time instant, the injected current is constant and the APV output voltages should follow a pattern for all the channels as those depicted in Fig. 8. Setting three different time instants along the injected sine-wave signal, t=t1 coincident with the positive peak, t = t2, coincident with the zero crossing and t = t3 coincident with the negative peak of the sine-wave, the simulated output voltage for all the 512 channels is depicted in Fig 9A for the TEC detector. In Fig. 9B the measurement at the same sampling times of the same output voltages are shown. It is important to observe the similarity between the measurements and the simulation results. Comparing the simulation and the measurements for the TOB detector, it is possible to obtain similar results. They are depicted in Fig. 10.

If the digitized output voltage of the APVs are further processed to measure the root-mean-squared (RMS) values of each channel, the RMS voltage distribution for all the detectors channels changes. Mainly, negative values in previous plots (Figs. 9 and 10) became positive when the RMS value is calculated. Figs. 11B and 12B depict the measured RMS output voltage of the APVs when a perturbing common mode current is injected through the ICB. The base noise in those plots is defined by the intrinsic thermal noise of the APVs. Plots have showing the RMS output voltage versus the 512 channels of the silicon detector have particular shape called by the CMS collaboration "wings". Proceeding with the calculations based on the model and simulation, the resulting RMS output voltage is depicted in Figs. 11A and 12A.

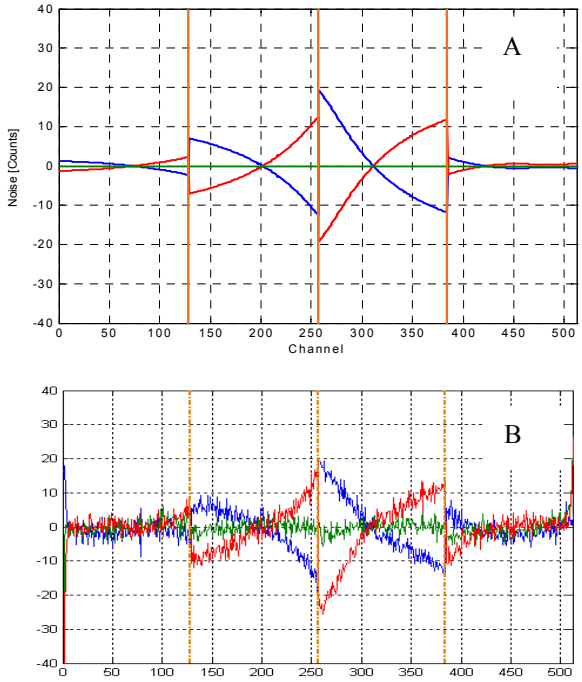

Figure 9: APV Digitized output voltage distribution per channel after common mode subtraction for TEC detector- t=t1 (red), t=t2 (green), t=t3 (blue) *A:* (simulated values) - *B:* (measured values).

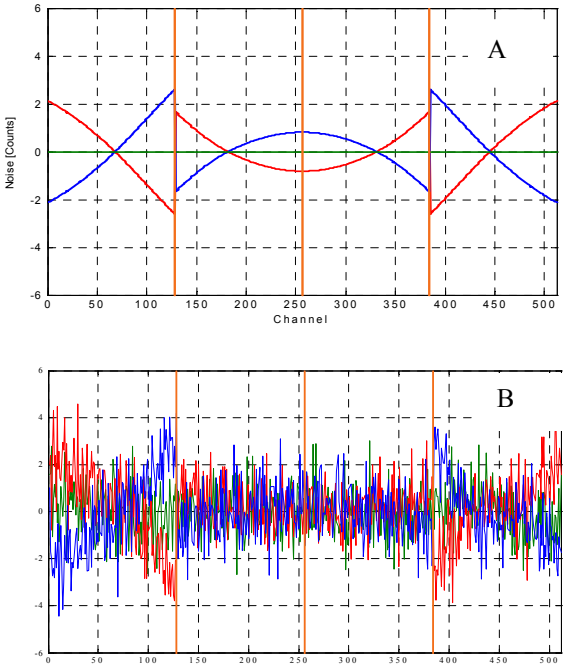

Figure 10: Digitized APV output voltage distribution per channel after common mode subtraction for TOB detector- t=t1 (red), t=t2 (green), t=t3 (blue)A: (simulated values)- B : (measured values)

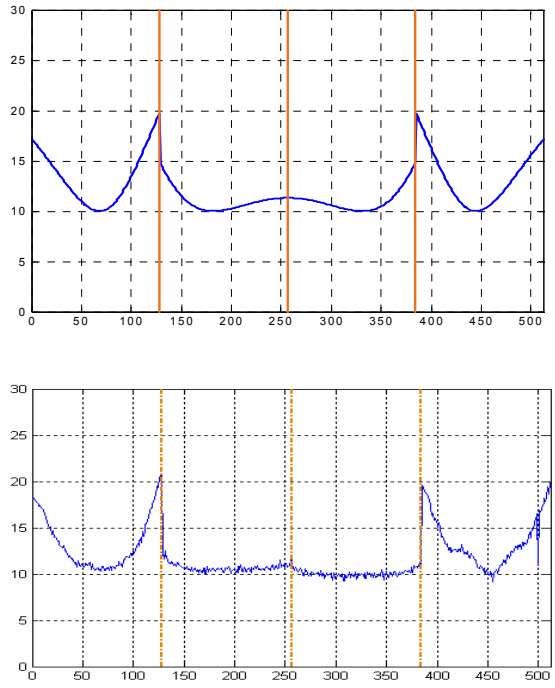

Figure 11: APV RMS output voltage distribution per channel after common mode subtraction for TOB detector – *A (upper):* (simulated values)-*B (lower):* (measured values)

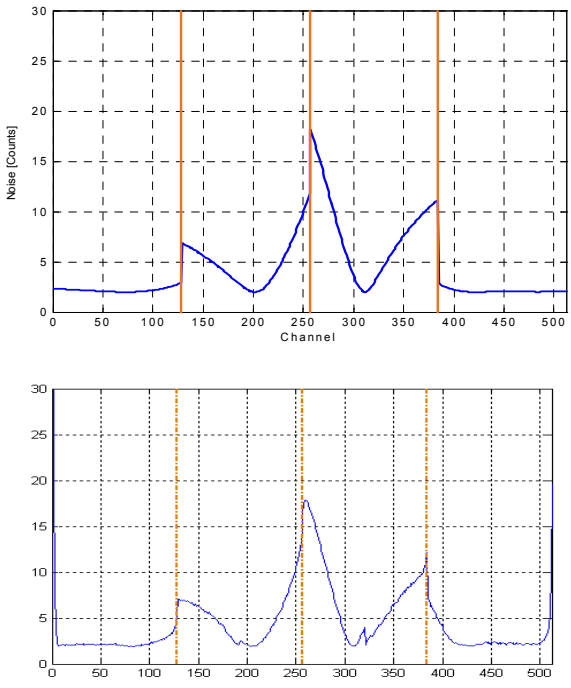

Figure 12: APV RMS output voltage distribution per channel after common mode subtraction for TEC detector – *A(upper):* (simulated values)-*B (lower):* (measured values)

VII. CONCLUSIONS – SLHC EFFECTS

A model of the coupling mechanism between the interference currents flowing in the ICB and the detector module have analyzed. Agreement is shown between simulations results based on the model and measurements on prototypes of two different CMS tracker systems. These studies and the model suggest that the improvement in the tracker module immunity can be achieved by minimizing the signal return loop around the pitch adapter. An integral mechanical design that connects the silicon detector back-plane and the hybrid board reference will force to flow the return current beneath the signal current minimizing the input signal loop. Another important point is that basic coupling is due to near electromagnetic fields, then minimizing, by design, the field radiated by the ICB will improve the overall immunity of the tracker's leather or petal. Additionally, filtering the interference currents at the input terminals of the distribution board will reduce the magnitude of the radiated fields.

VIII. ACKNOWLEDGMENT

The authors would like to thank to Dr. Peter Sharp from Imperial College/CERN for helping us during the development of these studies. Also, we would like to thank to Instituto Tecnológico de Aragón (ITA), Zaragoza, Spain and specially Dr. J.L. Pelegay, head of Grupo de Investigación Aplicada (G.I.A.) for the support of this work. Finally, one of us (C.R.) wants to thank to US DOE, under contract DE-AC02-76SF00515, for the support of this work..

IX. REFERENCES

[1] M. Raymond, et. al., "*The APV25 0.25 µm CMOS readout chip for the CMS Tracker*", Proc. IEEE Nuclear Science Conference, October 2000, Lyon, France, pp. 9/113 - 9/118

[2] F.Arteche, C. Rivetta, C. Esteban et al "*Detector noise susceptibility issues for the future generation of High Energy Physics Experiments*", Proceedings of Workshop on Electronics for LHC Experiments – TWEPP 2008, Vol 1, pp533-538, September 2008.

[3] F. Arteche, C. Rivetta and F. Szonsco, "*Electromagnetic Compatibility Plan for the CMS Detector at CERN*", Proc. of 15th Int. Zurich Symposium on EMC, February 18-20, 2003, Zurich, Switzerland, pp. 533-538.

[4] F.Arteche and C. Rivetta, "*Electromagnetic Compatibility Test for CMS experiment*", Proceedings of Workshop on Electronics for LHC Experiments – LECC 2002, Vol 1 , pp191-196, September 2002.

[5] F. Arteche and C. Rivetta "*EM Immunity studies for front-end electronics in high-energy physics experiments*", Proc. of Int. Symposium on EMC, EMC Europe 2004. September 2004, Eindhoven, The Netherlands, pp. 533-538.

[6] F.Arteche, C. Rivetta,"*EMC phenomena in High Energy Physics Experiments: Prevention & Cost savings*", Proceedings International Symposium on the Development of Detectors for Particle and Synchrotron Radiation Experiments – SNIC 2006: pp 0149. SLAC-R-842, April 2006

[7] M.Johnson et Al." *Electrical properties of carbon fiber support systems*", Nuclear Instruments and Methods in Physics Research Section A: Accelerators, Spectrometers, Detectors and Associated Equipment, Vol. 550, Issues 1-2,Sept 2005, Pages 127-138.